AIAA JOURNAL
Vol. 47, No. 5, May 2009

Simulation and Optimization of Flow Control Strategies for Novel High-Lift Configurations

M. Meunier*
ONERA, 92190 Meudon, France

DOI: 10.2514/1.38245

A kriging-based optimization algorithm is presented and applied to the design of a novel high-lift airfoil with a simply hinged, slotless flap and equipped with fluidic flow control. The position, orientation, and continuous-blowing characteristics of the actuator are set as design variables for the maximization of lift in landing conditions. Comparisons with a fully slotted reference configuration are presented and conclusions are drawn. In particular, it is found that a careful parameterization of the jet is capable of an efficient control strategy and leads to a complete reattachment of the flap flow, with considerable gains in lift and aerodynamic efficiency. A functional analysis of variance demonstrates the possibility of a dimensional reduction in the problem formulation and allows for a more in-depth analysis of the mechanisms governing separation management and alleviation in that particular case.

Nomenclature

C_l	=	lift coefficient
C_p	=	pressure coefficient
C_μ	=	jet momentum coefficient
$E[I(.)]$	=	expected improvement criterion
l_{ref}	=	reference length
M_∞	=	freestream Mach number
N	=	number of samples
P	=	number of variables
Re_j	=	l_{ref}-based Reynolds number
VR	=	jet to local isentropic velocity ratio
V_{inj}	=	injection velocity
$V_{\text{isentropic}}$	=	isentropic boundary velocity
V_x	=	streamwise velocity
V_∞	=	freestream velocity
x_{inj}	=	injection abscissa
y^+	=	normalized first cell height
α	=	angle of attack
δ	=	boundary-layer thickness
δ_{flap}	=	flap deflection angle
δ_{inj}	=	injection angle

I. Introduction

THE requirement for aircraft manufacturers to meet increasingly stringent regulations has pushed industrials and applied researchers toward the in-depth evaluation of innovative design strategies for boundary-layer separation delay or prevention. In this context, active flow control [1–3] is unanimously regarded as a key evolution, offering new solutions for the performance maximization of existing designs, and, to an even greater extent, the apprehension of new concepts, in which it could be used in a multidisciplinary approach, fully integrated to the initial screening and conception phases.

In 1999, McLean et al. [4] examined some of the benefits to be gained from the introduction of unsteady excitation to civil transport aircraft aerodynamics, ranging from exhaust mixing to engine inlet or landing-gear applications. They identified high-lift separation control as one of the most promising and feasible applications through the enhancement of conventional designs [5] or the suppression of slotted flaps. Applying flow control to such cases could not only improve takeoff lift-to-drag ratio and landing maximum lift, but could also result in drastic reductions in radiated noise, mechanical complexity, weight, manufacturing time, and costs from simplifications and/or size reductions relative to current systems.

High-lift devices consisting of simply hinged, moveable slats and/or flaps have had the interest of a growing number of studies in fairly recent years. Seifert et al. [6] conducted wind-tunnel tests on a NACA 0015 airfoil equipped with a 25% chord-length flap deflected up to 40 deg. Actuation in the form of steady/unsteady blowing was applied from a two-dimensional slot located on the suction side of the profile, above the flap pivot. A significant lift augmentation was observed, together with a cancellation of form drag and no adverse effects from Reynolds number increase. The superposition of an unsteady component was also seen to reduce mass flow requirements by 1 order of magnitude compared with steady-only blowing. Nishri and Wygnanski [7] and Darabi and Wygnanski [8,9] experimentally studied flow reattachment over an inclined plane surface simulating a simple flap, with similar conclusions. They reported, however, on the presence of a strong hysteresis effect and, as such, the existence of a dual management scheme (in which it is actually less expensive to maintain an attached flow for increasing flap deflection angles than it is to force reattachment at a given inclination), which ultimately pushes for closed-loop separation control [10]. With the aim of reducing blade–vortex interaction noise in helicopter applications, Hassan [11] performed unsteady thin-layer Navier–Stokes computations over a NACA 0012 airfoil with a 20% chord-length flap, deflected at 40 deg, and equipped with an oscillatory air jet at the upper flap shoulder. Partial flap reattachment was achieved. The author indicates that whereas the importance of transition and turbulence modeling remains of primary concern for Reynolds-averaged Navier–Stokes (RANS)-based simulations of controlled flows, the latter are capable of capturing global flow features with enough fidelity for general aerodynamic trends to be extracted. A parametric study also demonstrated that the expected aerodynamic benefits were mostly dependent on the jet peak Mach number and oscillating frequency (which are intrinsic characteristics of the actuator itself), rather than the injection angle. It is to be noted, however, that these computations do not account for the presence of a cavity below the orifice, which has since been shown to be of fundamental importance for trustworthy comparisons to be made [12].

In a first attempt to combine leading- and trailing-edge separation control, Greenblatt [13] performed experiments on a rectangular

Presented as Paper 4276 at the 25th AIAA Applied Aerodynamics Conference, Miami FL, 25–28 June 2007; received 24 April 2008; revision received 2 February 2009; accepted for publication 8 February 2009.

*Aerospace Engineer, Applied Aerodynamics Department; mickael.meunier@onera.fr.

planform wing equipped with three equal-span flaps hinged at 70% of a NACA 0015 airfoil. Unsteady control is provided by two independently operated bidimensional slots located at the leading edge (and behaving, to some extent, as a conventional leading-edge device) and at the upper flap-shoulder (equivalent to an additional flap deflection) of the wing. An important factor for maximized control efficiency was found in the operating phase shift between each actuator, in which aft suction should be applied when the upcoming shear layer (generated by the forebody excitation) sits closest to the flap surface. The effects of finite span and sweep angle (which is known to affect stall occurrence from an inboard to a tip mechanism in high-lift conditions) were also reported and discussed [14]. Using adapted sweep relations, a simple trajectory model was derived to explain the loss of control effectiveness in the tip region, with leading-edge actuation. Flap-shoulder control yielded some performance improvements, but with a significant loss of efficiency when compared with the unswept case. On the contrary, finite span effects seemed to have little influence against two-dimensional results.

Galbraith [15] performed unsteady RANS (URANS) simulations of the flow around a novel high-lift airfoil with a conventional slotted slat and a simply hinged flap deflected at 40 deg. Separation control was performed via an unsteady surface boundary condition applied near the flap shoulder. A parametric study, interested in the influences of injection angle, frequency, jet velocity average, and amplitude, was presented and discussed for different blowing characteristics (pulsed blowing, pulsed suction, and zero net mass flux). In general, the computations were found to be in good agreement with already available experiments. Lift improvements were reported, but flowfield analysis suggested that a single momentum source might not be capable of fully reattaching the flap flow for reasonable magnitude inputs. In the frame of the Adaptive Flow Control Vehicle Integrated Technologies (ADVINT) program, Kiedaisch et al. [16] conducted two- and three-dimensional (swept wing) experiments on a series of high-lift designs (conventional slotted slat, cruise, and drooped leading edges and slotted or simply hinged flaps), actuated at several locations and backed up by a computational fluid dynamics (CFD) survey by Shmilovich and Yadlin [17] (see also the work by Nagib et al. [18] for a discussion on similarity parameters). To meet their performance goals, the authors suggest that a jet-to-local-velocity ratio beyond two would be required, which could not be achieved for the leading-edge part. On the other hand, the use of active flow control near the flap shoulder, although not capable of complete reattachment, was seen to improve the complete airfoil performance. Eventually, the introduction of a spanwise flow component did not alter flow control efficiency, as also demonstrated by Seifert and Pack [19]. Computational results yielded the same conclusions with favorable comparisons against the experiments. Tests with distributed actuation were performed and showed that the combination of five equally spaced slots operating in phase could fully reattach the flow over the flap.

With the aim of gaining more understanding of the physics governing active control of highly separated flows, Nagib et al. [20] performed a numerical study on the same range of configurations. The authors identified four interdependent mechanisms as being responsible for lift enhancement: namely, separation and circulation controls, thrust vectoring of the active actuation, and surface pressure manipulation up to, and above, inviscid levels. In a companion series of small-scale experiments, Kiedaisch et al. [21] examined the influence of the dynamic deflection of a drooped flap and concluded on the independence of actuation effects on deflection rate, up to the angle at which separation could not be fully alleviated anymore and for which static control outperformed the dynamic one.

In a series of publications, Pack Melton et al. [22–24] presented wind-tunnel measurements on a supercritical airfoil fitted with a 15 and 25% chord length simply hinged slat and flap. Synthetic control was applied at several leading- and trailing-edge positions, and tests with combined actuated locations were performed. Overall, it was found that larger momentum inputs are required for an effective management of the flap separation (when compared with the slat counterpart), with emphasis put on the importance of surface curvature. Encouraging results were also reported from synchronous fore and aft excitations. Khodadoust and Washburn [25] and Khodadoust and Shmilovich [26] presented a combined experimental/computational study of the same airfoil equipped with a slotted flap (in lieu of the simply hinged one) at higher Reynolds numbers (up to 9×10^6). The effect of that last parameter was found to be significant indeed, suggesting that the assessment of control performance be conducted at near flight-scale conditions. Furthermore, and without looking at actuation power requirements, steady active control provided better maximum lift increments than zero-mass-flux input. Again, a satisfactory agreement is reported between wind-tunnel tests and simulations, specifically in the linear lift range.

Although appealing, the suppression of the slat and flap slots is not as easy as it would originally appear. They are important elements in which the entire performance of conventional high-lift configurations are to be found [27], from limitations to local pressure rises (the primary cause of flow separation) and a more homogeneous repartition of the airfoil loads over its three (or more) elements. Adding the presence of rapid and rather severe geometry changes to the loss of these highly elliptical effects, it is easy to understand that the aerodynamic behavior of uncontrolled slotless geometries is relatively poor in its original basis, being subject to massive separations and early stall.

Although the preceding investigations demonstrate various degrees of improvements from the introduction of flow control concepts, the sensitivity of aerodynamic performance to design choices makes it a nontrivial and certainly expensive problem, the number of actuation parameters and combinations thereof being almost infinite. As a possible answer [28,29], a completely automated, surrogate-based optimization [30,31] algorithm was developed and applied to the design of a two-dimensional high-lift system with a conventional slotted slat and a simply hinged, slotless flap. The process will now be described in detail and results for a continuously blowing slot will be presented.

II. Overview of the Optimization Process

A general flowchart for any surrogate-based optimization loop is presented in Fig. 1. Details for each individual procedure are given in the following sections. The framework of this algorithm, which has been extensively validated over a series of analytical test

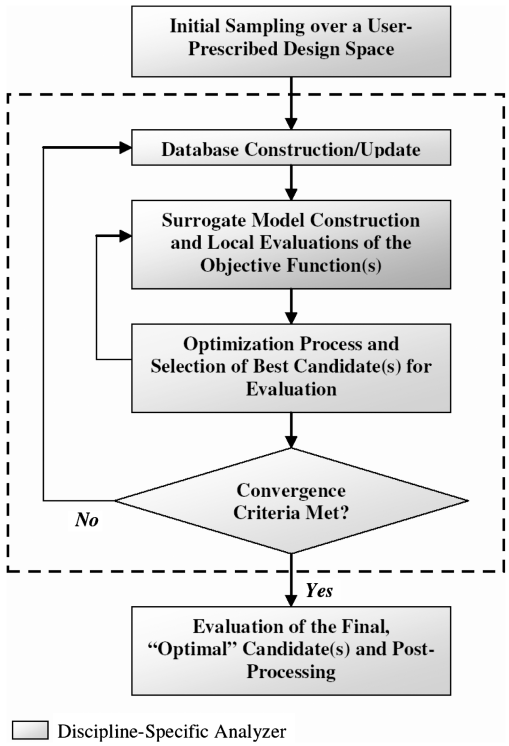

Fig. 1 Outline of surrogate-based optimization algorithms.

problems (see [32] for corresponding complements), is a collection of FORTRAN/Shell routines encompassed in a Python computer language interface.

A. Sampling

The construction of a surrogate model of any black-box function requires the creation of a database of precisely evaluated individuals. By database, we mean a collection of samples, spread all over or slightly outside the design space of interest, which should be as representative as possible of the interactions existing between the design variables on the one side and the objective functions to be optimized on the other side. It is of fundamental importance for the sampled points to be distributed homogeneously across the search space so that no region is left without a single representative. The apparition of design-of-experiments concepts has introduced a large number of sampling methods, including fully random, Monte Carlo, Tagushi, Halton/Hammersley, central Voronoï tessellation, or Latin hypercube, each with its advantages and drawbacks [33,34]. Among these, the constrained space-filling Latin hypercube sampling (LHS) was chosen for its simplicity and yet good overall performance compared with other, more complex, formulations. In the case in which we wish to gather N samples of P variables [where $N \geq (3 \text{ to } 10)^P$ is a first rule of thumb for a correct initial representation], the LHS strategy is performed as follows:

1) Divide the range of each variable into N nonoverlapping equal-probability (hence equal-size) intervals.

2) From a user-specified (usually uniform) probability density, arbitrarily select one value from each interval in every direction and randomly couple (equally likely combinations) the N values of each dimension.

B. Design Analyzer: RANS CFD Flow Solver

The computational method used in this study relies on ONERA's structured, multiblock, cell-centered, elsA CFD software [35]. The Reynolds-averaged form of the Navier–Stokes equations is solved using the Jameson et al. [36] second-order centered scheme with artificial viscosity for the spatial discretization. The implicit phase is resolved using a lower/upper symmetric successive over-relaxation technique, and convergence is accelerated through a one-level, v-cycle, multigrid algorithm combined with low-speed preconditioning. Turbulence closure is achieved under a Boussinesq hypothesis using the one-equation model of Spalart and Allmaras (SA) [37]. Precise, fully turbulent, boundary-layer resolutions ensured average y^+ (based on the height of the first wall-bounded cell) values below unity for all of the meshes considered here. To keep the overall computational cost of the procedure as reasonable as possible, and bearing in mind that design definitions based on automated optimization are concerned mainly with precise trends and performance variations between each design point (rather than their precise performance assessment, as such, provided that the correct physics of the phenomena to be modeled is effectively captured), steady-state solutions were obtained using a quasi-stationary backward-Euler integration with a Courant–Friedrichs–Lewy number-derived time step. For all cases, a thorough iterative convergence study (on residuals, forces, and moments) guaranteed that fully converged solutions were obtained. The prediction capabilities of the software for isolated [38] and flow-control-enhanced [5] high-lift problems have been reported already and will not be further discussed here.

C. Surrogate Model (Response Surface Method)

The major disadvantage of classical optimization techniques is the important computational cost of the high-fidelity analyzer at each objective-function evaluation. An alternative is the construction of a response model that links the design variables with the inputs for the optimizer (i.e., objective functions) through a simple and inexpensive, yet accurate, relation. The most widely used substitute models include multilayer perceptron or radial basis functions [39] neural networks, polynomial-based formulations, and, gaining increasing popularity, the kriging linear interpolation method, as formulated in its ordinary form by Sacks et al. [40].

Let us consider a globally unknown function Y, expressed as a stochastic process:

$$Y(x) = \beta + Z(x) \tag{1}$$

where x is the P-dimensional vector of design variables; β is a global constant of the model (its mean); and $Z(x)$ represents an error, or deviation, term assumed to have mean zero and covariance (COV)

$$\text{COV}\,(Z(x_i), Z(x_j)) = \sigma^2 \cdot R(f(x_i, x_j)) \tag{2}$$

between $Z(x_i)$ and $Z(x_j)$, where σ^2 is the process variance and R a symmetric, $N \times N$ correlation matrix with ones along the diagonal. The strongest hypothesis of this method if the choice of f as a user-specified, predefined, correlation function.

To estimate the random components of Y, the N original (LHS) sample points are interpolated using a Gaussian correlation function. This makes them closely dependent on the relative distance between each design sites, $d(x_i,x_j)$. Instead of an Euclidian distance, that would weight all the variables equally, the following norm is employed:

$$d(x_i, x_j) = \prod_{k=1}^{P} \theta^k \cdot |x_i^k - x_j^k|^2 \tag{3}$$

where $\theta^k > 0$ is a correlation parameter vector, or, if deemed sufficient constant (as in the case here, hence the isotropic nature of the surrogate) to be determined.

Based on that, the Gaussian correlation function between the errors at x_i and x_j becomes

$$f(x_i, x_j) = e^{-d(x_i,x_j)} \tag{4}$$

Now, let r denote the N vector of correlations between the estimation error at x^*, an untried design set, and the error terms at the already known points.

The derivation of the kriging predictor, not discussed here, yields the following estimation of Y (marked $\hat{y}$) at x^*:

$$\hat{y}(x^*) = \hat{\beta} + r^T.R^{-1}.(y - 1.\hat{\beta}) \tag{5}$$

where $\hat{\beta}$ is an estimation of β and y the true value of Y at each sampling point. The determination of the $P + 2$ unknown parameters $(\theta, \beta, \sigma^2)$ is such that they maximize the log-likelihood of the samples: that is, the log form of the maximum likelihood function (MLF) defined as

$$\text{MLF} = \max_{\theta,\beta,\sigma^2} \left[-\frac{N}{2} \cdot \ell_n(\sigma^2) - \frac{1}{2} \cdot \ell_n(|R|) - \frac{-(y - 1 \cdot \beta)^T \cdot R^{-1} \cdot (y - 1 \cdot \beta)}{2 \cdot \sigma^2} \right] \tag{6}$$

The corresponding estimates of β and σ^2 are

$$\hat{\beta} = \frac{1^T \cdot R^{-1} \cdot y}{1^T \cdot R^{-1} \cdot 1} \quad \text{and} \quad \hat{\sigma}^2 = \frac{(y - 1 \cdot \hat{\beta})^T \cdot R^{-1} \cdot (y - 1 \cdot \hat{\beta})}{N} \tag{7}$$

The preceding problem, dependent only on θ, is solved using the same unconstrained nonlinear optimization technique as employed for the global problem and described subsequently.

The quality of the prediction is obviously affected by the correlation of the errors, that is the distance between x^* and the reference points (the closer, the better). This is expressed in the following expression for root-mean-square prediction error (RMSE):

$$s(x^*) = \hat{\sigma} \cdot \left[1 - r^T \cdot R^{-1} \cdot r + \frac{(1 - 1^T \cdot R^{-1} \cdot r)^2}{1^T \cdot R^{-1} \cdot 1} \right]^{1/2} \tag{8}$$

Thus, a kriging interpolation is able to provide both an estimation of the objective function and some sort of uncertainty quantification

at untested design points, which is a clear advantage of the method compared with most of the other metamodels.

D. Optimizer

Among the many optimization strategies available (e.g., finite difference or adjoint-based gradients and descent, simulated-annealing [41], simplex or multidirectional search [28]), a derivative-free, genetic algorithm (see Fig. 2 for an overview), GADO [42], was preferred for the following reasons:

1) It is easy to interface with readily existing black-box solvers (or the kriging surrogate in this case),

2) It has better robustness and independence toward the choice of an objective function, especially in aerodynamic problems facing various levels of nonlinearity and/or discontinuities,

3) Its searching pattern is based on a population of individuals, making it less amenable to local minima entrapments.

Values for population size and number of generations were set to 50 and 20, respectively, with a mutation factor of 0.4, as suggested by previous studies.

III. Design of a Novel Airfoil Equipped with a Slotless Flap and Flow Control

This study is interested in the mono-objective optimization of flow control input for a two-dimensional section equipped with a single constant blowing nozzle (to be seen as a spanwise tangential slot in three dimensions) with a length-to-diameter aspect ratio of four. All the computations were performed at a chord-based Reynolds number of $Re_l = 2.33 \times 10^6$ (freestream Mach number of $M_\infty = 0.2$) and the optimization conducted at a single design point, for an angle of attack of $\alpha = 25$ deg, which corresponds to the stall incidence of a reference (conventional, three-element) geometry.

A. Airfoil Geometry

The latter is the GARTEUR AG08 high-lift landing configuration, for which extended experimental [43] and elsA computational results [37] have been obtained. This design was modified in its aft part to remove the trailing-edge slot and thus create a simply hinged flap, with a deflection angle of $\delta_{\text{flap}} = 25$ deg (to be compared with $\delta_{\text{flap}} = 32.4$ deg for the original flap) and articulated at 75% of its chord, as shown in Fig. 3.

B. Problem Parameterization, Meshing Strategy, and Objective Function

Variations in blowing characteristics are allowed through modifications to the injection abscissa x_{inj}; the injection angle relative to the local normal, δ_{inj}; and the injection speed V_{inj}, as displayed in Fig. 4.

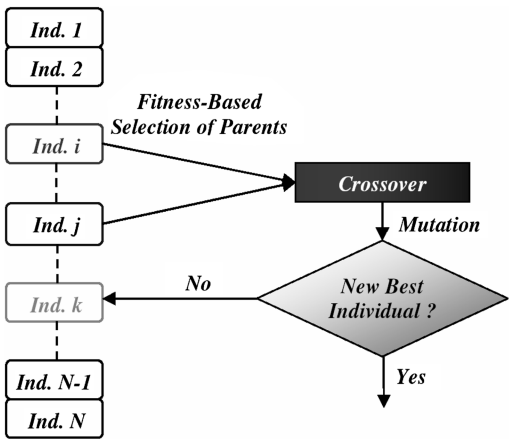

Fig. 2 Genetic algorithm optimization principles.

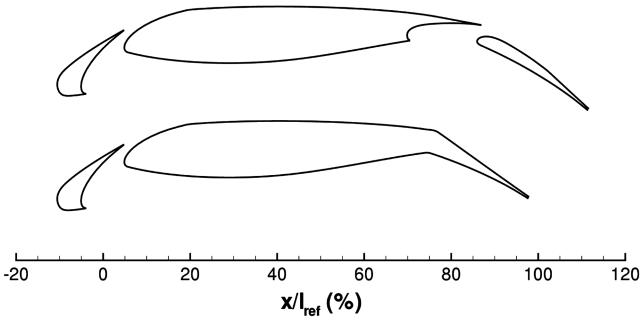

Fig. 3 GARTEUR [45] reference (up) and simplified (down) high-lift geometries.

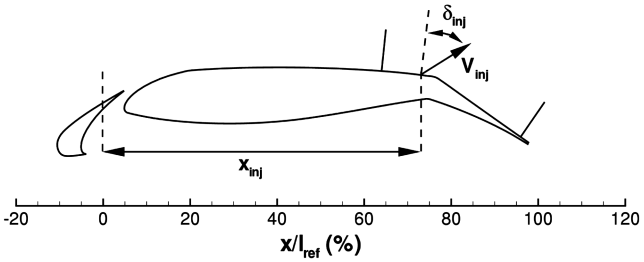

Fig. 4 Problem parameterization.

Design variables are allowed to fluctuate in the following ranges:

$$64 \leq x_{\text{inj}}/l_{\text{ref}} \leq 96\% \tag{9}$$

$$0 \leq d_{\text{inj}} \leq 70 \text{ deg} \tag{10}$$

$$0 \leq V_{\text{inj}}/V_\infty \leq 3.6 \quad \text{or} \quad 0 \leq C_\mu \leq 5.1\% \tag{11}$$

where

$$C_\mu = \frac{2 \cdot \rho_{\text{inj}} \cdot d_{\text{inj}} \cdot V_{\text{inj}}^2}{\rho_\infty \cdot l_{\text{ref}} \cdot V_\infty^2}$$

These values were chosen based on manufacturing and experimental constraints, given the current status in actuator's development and integration. The mesh, shown in Fig. 5, is generated on a partially automated component-build-up basis, using overset grids for the slat and injection slot (discretized analytically using the optimizer's output). The latter is linked to the background mesh through a body-conforming interfacing domain, which ensures a correct flux continuity at the slot exit. The actuator sits in a greatly refined region, resulting in a nominal bidimensional grid with approximately 170,000 nodes. A mass-flow-type fluid injection is imposed at the entrance of nozzle, whereas its lateral boundaries are treated under a no-slip hypothesis, which allows for some boundary-layer developments inside the cavity. The meshing strategy employed here imposes a sharp-edge integration of injection slot on the airfoil upper surface, which corresponds to manufacturing process currently in use for such configurations (and eases the automation of the process because the slot-profile interfacing does not change throughout the optimization and therefore does not require an a priori special treatment).

Because we are only interested in approach configurations, the primary objective of the optimization is to maximize lift coefficient, at least up to the performances of the baseline design. However, to overcome the difficulties underlined before regarding the importance of response surface representation and improvement, the preceding problem was transformed to balance the search for a global optimum with the need for extra-sampling at the locations of highest estimation uncertainty. To illustrate that, we introduce a conceptual monodimensional problem (Fig. 6). Let us suppose we want to find the minimum of a globally unknown function, based on the existing

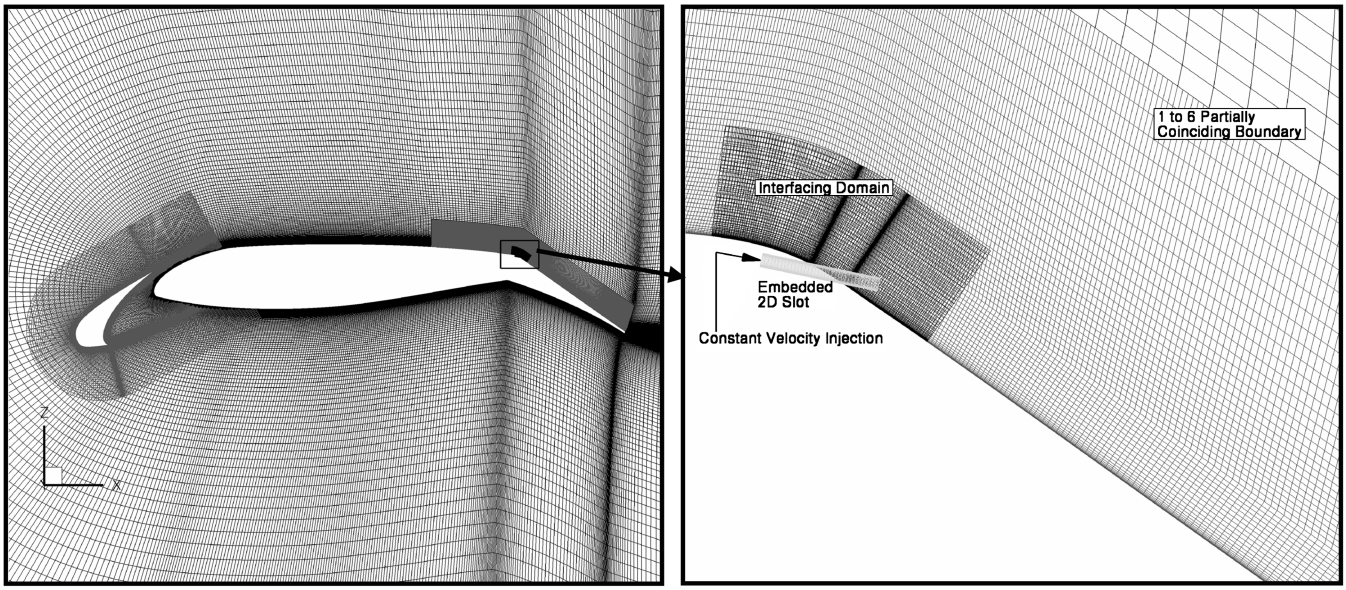

Fig. 5 Mesh arrangement showing the flow-control-input overlapping strategy.

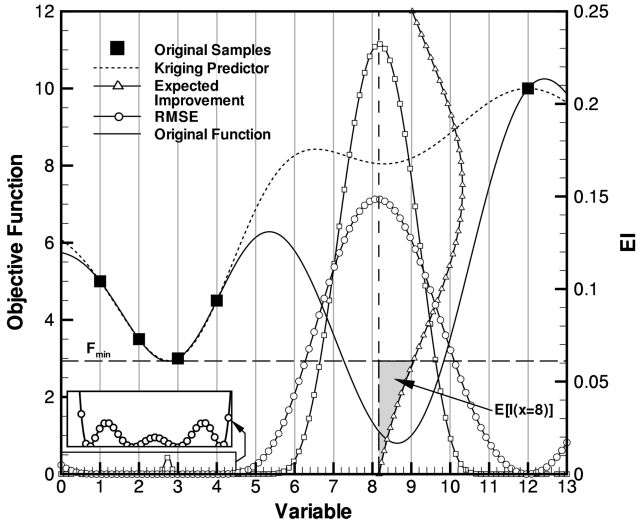

Fig. 6 An illustration of expected improvement principles.

samples shown subsequently. As discussed earlier, the resulting kriging interpolation is accurate around the initial population but becomes fundamentally false outside certain intervals, around $x = 8$ in this case, as proved by the shape of RMSE. Should one run an optimization on this kriging model, the optimizer will find the local minimum between $x = 2$ and $x = 3$, and call for a function evaluation at this position. As a result, the updated response surface will have the exact same shape as the original one and the global minimum be certainly missed. A high RMSE, on the other hand, suggests a good place to search from a global representation point of view, but sampling there would mean only improving the quality of the surface without actually looking for an optimum.

Jones et al. [44] propose a figure of merit that balances this need for a combined local and global search, the expected improvement (EI) criterion. If we model our uncertainty at some untried design point by a normal density function with mean and standard deviation suggested by the kriging model, the expected improvement represents the probability for the objective function at that point to be better (lower in that case) than the currently known minimum, $F_{\min}$. Mathematically, this can be expressed as

$$E[I(x)] = (F_{\min} - \hat{y}).\Phi\left(\frac{F_{\min} - \hat{y}}{s}\right) + s.\phi\left(\frac{F_{\min} - \hat{y}}{s}\right) \qquad (12)$$

where ϕ and Φ are the standard normal density and distribution functions, respectively. Also recall that s is the RMSE measure of Eq. (8). In this work, we define $\hat{y}$ as the ratio of uncontrolled to controlled lift, which we are looking at minimizing:

$$\hat{y} = \frac{C_{l,\text{uncontrolled}}}{C_{l,\text{controlled}}} \qquad (13)$$

C. Computational Results for the Reference and Uncontrolled Configurations

Before applying any form of separation control, the performance of the newly defined, uncontrolled geometry was evaluated and compared with the reference three-element case. By doing so, we obtained a measure of the lift deficit engendered by the suppression of the flap slot as well as preliminary guidance regarding possible actuator positioning, local boundary-layer thicknesses, recirculation topologies and equivalent isentropic boundary velocities.

The evolution of lift coefficient with angle of attack is presented in Fig. 7 for the baseline (with reference to higher Reynolds number ONERA F1 experiments by Manie et al. [45]) and uncontrolled cases, showing a 25 to 30% lift loss over the range of practical incidences. Turbulence modeling dependency was assessed through a comparison between SA [36] and Wilcox's [46] k-ω results over the complete incidence range, with added Jones–Launder's [47] k-ε and Menter's [48] k-ω with SST correction trials at the optimization angle of attack. Comparing the formers, the influence of the closure formulation is seen to be fairly negligible throughout the linear part of the polar and up to the maximum lift area, in which the two-equation model predicts a higher stall incidence. At $\alpha = 25$ deg, little to no changes are visible between the four turbulence models (given the lift levels encountered here), so that the SA model, which remains today's most popular choice in many industrial external aerodynamics applications, was eventually selected for all remaining simulations to be discussed hereafter.

A comparison of computational and experimental surface pressure distributions is also depicted at that angle of attack for the reference geometry and shows a very good agreement over the three elements, as expected from similar previous validation studies [5], with somewhat limited Reynolds number effects (main element trailing-edge).

Figure 8 depicts the evolution of surface pressure coefficient with angle of attack. It is interesting to note that the pressure levels are almost independent on incidence over the aft part of the airfoil (downstream $x/l_{\text{ref}} = 50\%$). For that particular case, the onset of trailing-edge separation is not driven by increasing pressure

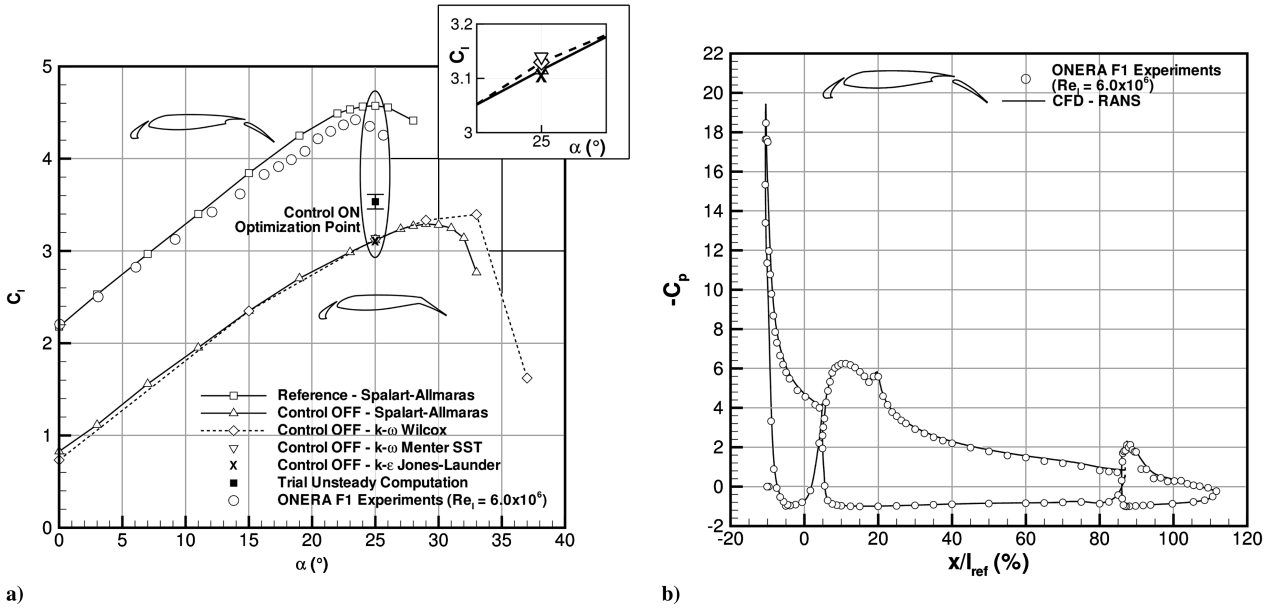

a) b)

Fig. 7 Plots of a) lift coefficient vs angle of attack for the reference and uncontrolled cases and b) corresponding reference pressure distributions at $\alpha = 24$ deg.

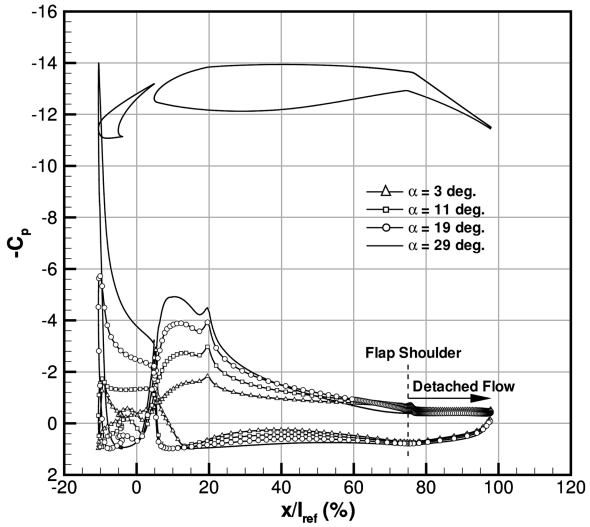

Fig. 8 Evolution of surface pressure distribution with incidence for the uncontrolled case.

gradients (which is usually the case for conventional high-lift devices), but by invariant geometrical constraints, in which the flow is unsuccessfully forced to take a sharp turn around the upper flap shoulder. When looking at a typical flowfield, it can be seen that the general topology observed in Fig. 9 remains basically unchanged with increasing angles of attack, which suggests that a one-design-point ($\alpha = 25$ deg here) optimized control scheme should also be effective at offdesign conditions (given that boundary-layer alterations remain moderate with varying incidences).

Figure 10 illustrates the evolution of boundary-layer thickness above the main-element suction side, together with isentropic surface velocities. Note that the complex slat wake/main-element boundary-layer confluence makes it actually difficult to evaluate precisely, which explains the fluctuations observed between $x/l_{\text{ref}} = 40$ to 60%. Over the attached aft part of the airfoil, and within the range of interest for possible flow control input, the height of the boundary layer varies from approximately 10 to 20 mm, giving us a ratio of $l_{\text{slot}}/\delta \in [0.05, 0.1]$, in the average of what is commonly observed in most existing studies. With our maximum injection speed, a ratio of jet to local velocity of up to VR = 3 will be permitted inside the controllable area, which is similar to already available experimental setups and results found in the literature.

D. Steady Versus Unsteady RANS Results for the Uncontrolled Case

It is a well-known fact that flow separation is an unsteady, usually three-dimensional, process: at the very least, one would expect to encounter some form of vortex-shedding behind such configurations at this range of Reynolds numbers, which the preceding

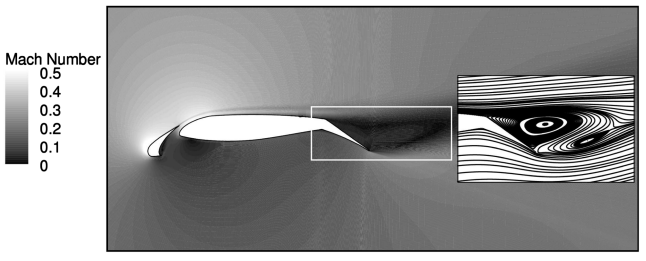

Fig. 9 Contours of Mach number and associated streamlines for the uncontrolled case.

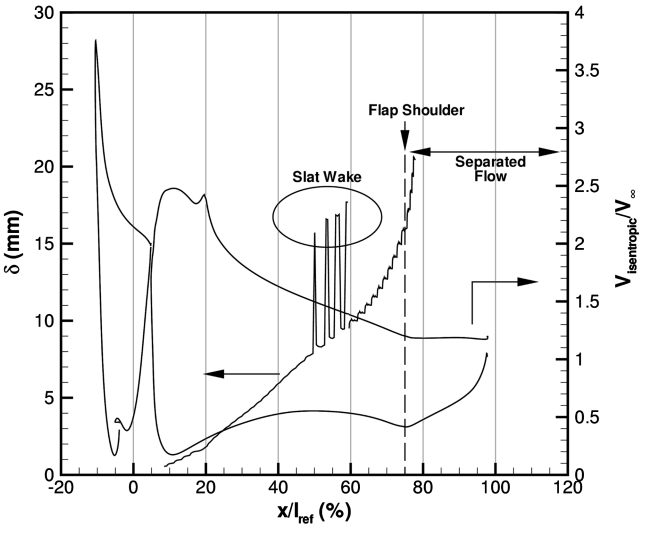

Fig. 10 Suction-side boundary-layer thickness and isentropic surface velocities for the uncontrolled case.

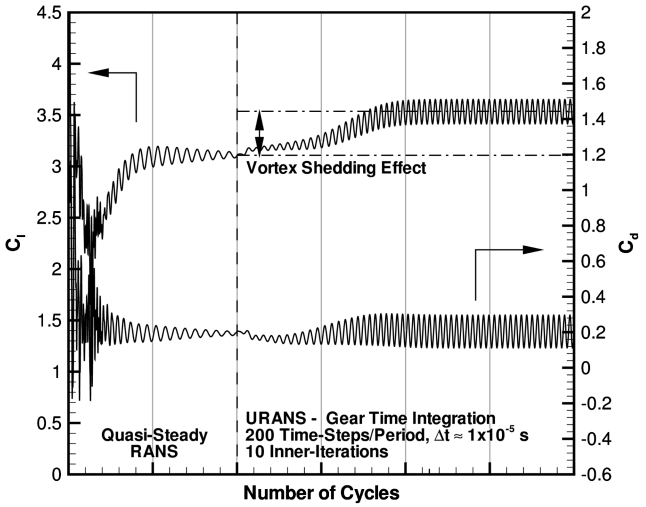

Fig. 11 Convergence of steady/unsteady lift and drag coefficients for the uncontrolled case at $\alpha = 25$ deg.

computations does not exhibit. Hence, decision was made to perform a time-accurate simulation at the chosen design point, to try to assess the quality and veracity of our steady CFD hypothesis as well as turbulence model choice for the upcoming, computationally intensive optimization environment. The resulting convergence history is plotted in Fig. 11.

The URANS computation is initiated using a steady RANS solution (from an average value point of view) and a second-order accurate Gear [49] temporal scheme with 10 inner iterations (guaranteeing at least a 3 orders of magnitude decrease of the inner residuals) and 200 physical time steps per characteristic period is employed. A transient departure is observed for lift and drag coefficients, corresponding to the capture of a well-established vortex-shedding phenomenon, at a frequency of approximately 150 Hz (or a circulation height-based Strouhal number of $St_h = 0.125$). When averaged in time, this corresponds to a reduction in the extent of the separated region which is translated into a lift increment (from circulation effects), as shown in Figs. 7 and 12 in which an instantaneous as well as mean time flowfield is represented. The backflow regions are seen to be mostly equivalent in shape and topology, with a separation point imposed entirely by the strong curvature at the flap shoulder. Galbraith [15] obtained similar conclusions.

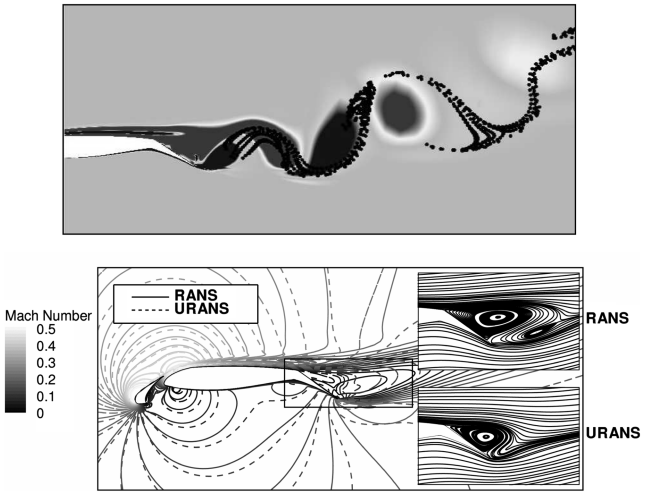

Fig. 12 Instantaneous contours of crossflow vorticity and associated particle paths for the unsteady uncontrolled case (up) and Mach number contours/streamlines for the RANS and time-averaged URANS scenarios (bottom), at $\alpha = 25$ deg.

Yet, because of the huge computational times involved (at least 2 orders of magnitude superior to that of the steady RANS approach), it would have been very expensive to perform fully URANS-based objective-function evaluations. Moreover, because the application of flow control is supposed to delay or even alienate flow separation, the sources of possible unsteadiness will be equally absorbed as the optimization progresses, which should allow for steady computations to be realistically retained (again, one is mostly concerned with the relative variations of performance between each design proposed by the optimizer). For that matter, it was decided that the steady-result uncontrolled lift coefficient be kept as a reference in the evaluation of EI.

E. Optimization Results and Discussion

1. Sampling and Modifications to the Algorithm (Hybridizing)

The construction of the initial kriging model is based on a LHS-collection of $3^3 = 27$ samples. The optimization procedure has been slightly modified to account for the introduction of EI as the objective function. To begin with, 100 EI designs are added to the database using GADO. The selection of parents for crossover and mutation uses a pool of 50 individuals, and up to 2000 kriging-based inner optimization iterations are allowed for each of the 100 outer function evaluations. The best result is then selected as a starting point for a small number (typically 5 to 10 iterations to reach convergence) of finite difference gradient-based descents using CFSQP [50] and Eq. (13) as the function to minimize. This whole process ensures a correct and global surface enrichment while further seeking improved quality in a more local fashion [51].

2. Assessment of Convergence and Kriging Model Validation

The convergence history in the course of the optimization is shown in Fig. 13, with the corresponding lift coefficient interpolation (on a 51^3 Cartesian grid) in Fig. 14. In all, 130 RANS simulations were conducted throughout the procedure, and increasing the number of process iterations did not yield any performance improvement. It can be seen that the use of EI produces a very scattered final population (which explains the hectic evolution of lift with the growing number of function evaluations), while still putting emphasis on the search for a best individual, a behavior that was definitely sought.

Similar conclusions can be made by looking at cross-validation results [52] (Fig. 15). The aim is to validate the resulting response surface as an accurate representative of the problem to be solved, by leaving out one of the original observations and predicting it back using only the $N - 1$ remaining points. If the model was perfectly exact, the representation of the true objective-function value against its cross-predicted counterpart should lie on a line with a unity slope.

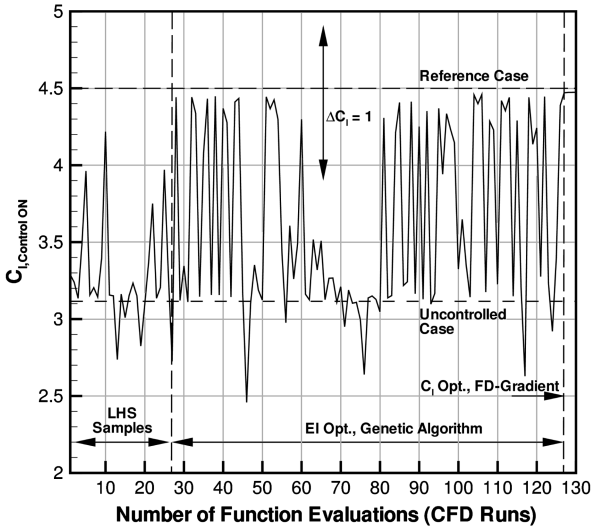

Fig. 13 Lift coefficient convergence history during the optimization process.

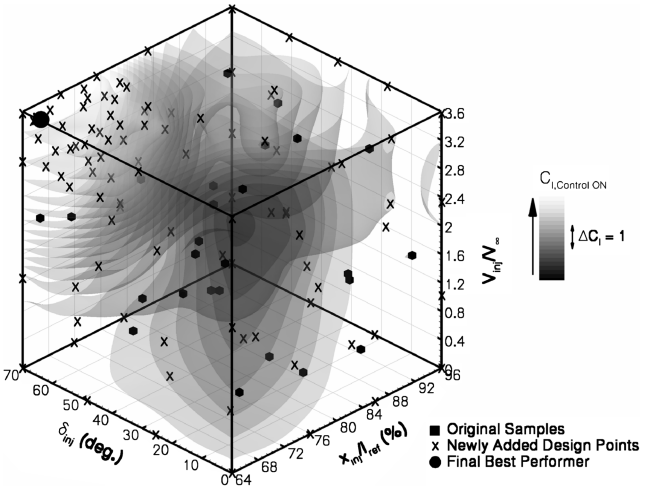

Fig. 14 Sampling evolution and resulting kriging interpolation for lift coefficient at the end of the optimization.

In our case, the samples are almost uniformly distributed across the achievable performance range and well gathered around a linear regression line, indicative of a relatively strong relationship, especially with an isotropic formulation [every direction (i.e., variable) is treated with the same correlation parameter]. Moreover, very little regularization was needed to interpolate the data, suggesting that the kriging surrogate we obtained is sufficiently accurate and well representative of the problem we are modeling.

3. Best-Performing Candidate

Flow control parameters for the highest-lift design were found as follows:

$$x_{\text{inj,opt}}/l_{\text{ref}} = 64.5\% \tag{14}$$

$$\delta_{\text{inj,opt}} = 66.5 \text{ deg} \tag{15}$$

$$V_{\text{inj,opt}}/V_\infty = 3.6 \quad \text{or} \quad C_m = 5.1\% \tag{16}$$

Figure 16 depicts Mach number contours, together with the resulting streamline arrangement for the optimal controlled scenario, to be compared with the baseline configuration displayed in Fig. 9. The result is a complete flow reattachment over the flap and a large modification of the overall flow pattern following the substantial downwash increase at the flap trailing edge. The main-body leading-edge velocity peak effect is now extended toward the flap shoulder, with important benefits in terms of pressure distribution, as shown in Fig. 17.

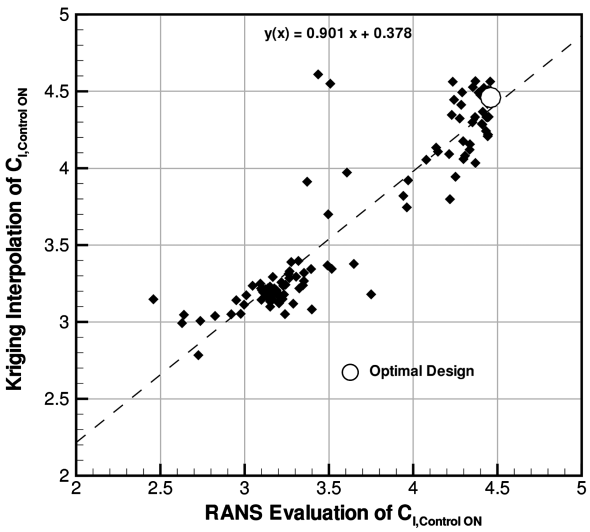

Fig. 15 Kriging cross-validation results for the high-lift optimization application.

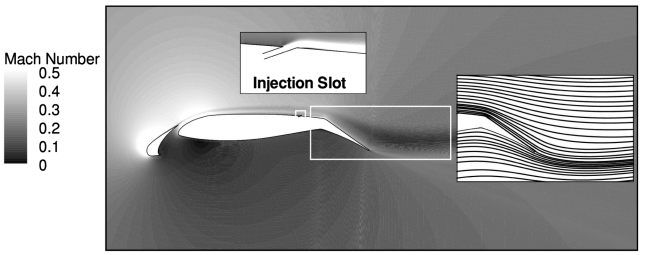

Fig. 16 Contours of Mach number and associated streamlines for the optimally controlled case.

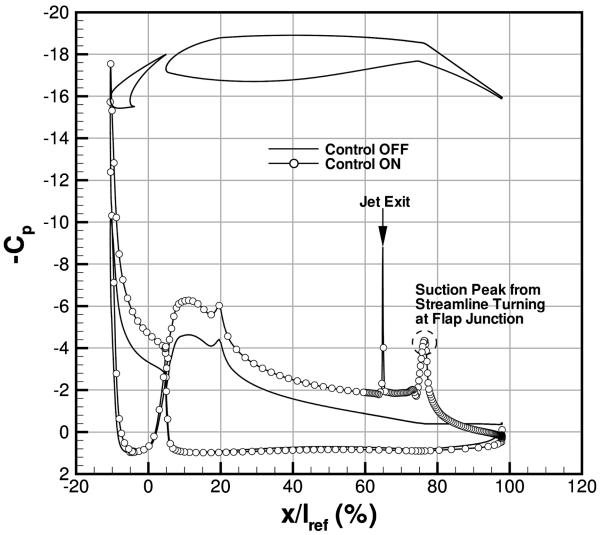

Fig. 17 Comparisons of surface pressure distributions for the uncontrolled and optimally controlled cases.

The consequence of momentum input is perceptible from the plot of boundary-layer profiles (Fig. 18). The velocity peak corresponding to the high-speed injection is propagated all the way downstream, despite the strong pressure gradient to be sustained. Its normal extension, however, is quite limited, which is characteristic of a Coandà-like (blowing being almost tangential in our case) circulation control [53] effect (i.e., a balance between centrifugal forces and low static-pressure levels from the high-momentum introduction of the wall-bounded jet over the convex upper surface [54]).

The extent of control authority was assessed through an incidence sweep and comparisons of lift levels against the reference

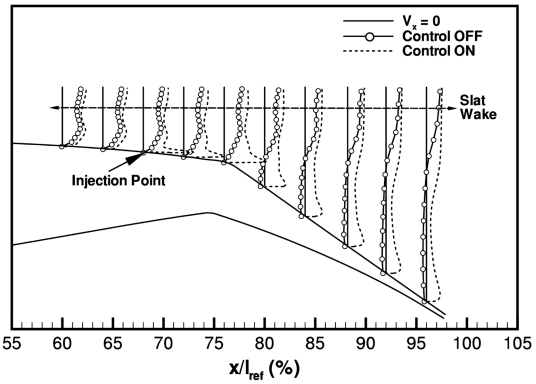

Fig. 18 Streamwise velocity evolutions for the uncontrolled and optimally controlled cases.

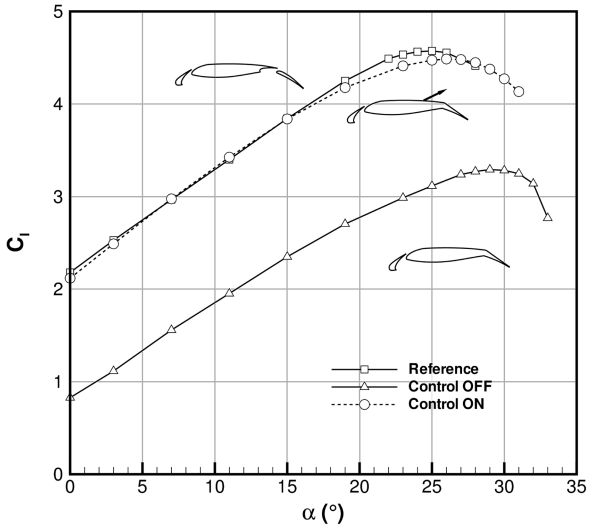

Fig. 19 Lift coefficient vs angle of attack for the reference uncontrolled and optimally controlled cases.

configuration (Fig. 19). The original goal and motivation behind the application of fluidic momentum input on that particular configuration (the recovery of the fully slotted reference performances at minimal costs) have been fully achieved over the entire incidence range. It should be noted as well that the controlled geometry has a 7.5 deg, unfavorable, flap deflection difference with the baseline geometry, and, contrary to the latter, does not benefit from chord extension, as the flap is unstowed. In fact, there is little doubt that in exactly similar operating conditions, the fittest sample proposed by the optimization procedure would perform even better than the reference does, which demonstrates the validity of our design framework on one hand and of separation-management concepts on the other hand.

4. Global Sensitivity Investigation: Functional Analysis of Variance

With the kriging surrogate model being an integrable function over its design hypercube Ω, Sobol' [55] showed that the estimation of a our objective function at design point x, $\hat{y}(x)$, could be represented in an analysis-of-variance (ANOVA) form:

$$\hat{y}(x) = \hat{y}_0(x) + \sum_i \hat{y}_i(x_i) + \sum_{i<j} \hat{y}_{ij}(x_i, x_j) + \cdots + \hat{y}_{1,\ldots,P}(x_1, x_2, \ldots, x_P) \tag{17}$$

where

$$\int_\Omega \hat{y}_{i_1,\ldots,i_s}(x_{i_1}, \ldots, x_{i_s})\mathrm{d}x_k = 0 \quad \text{for } k = i_1, \ldots, i_s \tag{18}$$

In Eq. (17), $\hat{y}_0(x)$ represents the total mean of the model, whereas $\hat{y}_i(x_i)$ can be viewed as the main effect of variable i, and $\hat{y}_{ij}(x_i, x_j)$ is the first-order interaction effect between variables i and j, and so forth.

It follows from Eq. (18) that the members in Eq. (17) are orthogonal and can be expressed as integrals of $\hat{y}(x)$:

$$\begin{cases} \int_\Omega \hat{y}(x)\mathrm{d}x = \hat{y}_0 \\ \int_\Omega \hat{y}(x)\prod_{k\neq i}\mathrm{d}x_k = \hat{y}_0 + \hat{y}_i(x_i) \\ \int_\Omega \hat{y}(x)\prod_{k\neq i,j}\mathrm{d}x_k = \hat{y}_0 + \hat{y}_i(x_i) + \hat{y}_j(x_j) + \hat{y}_{ij}(x_i, x_j)\cdots \end{cases} \tag{19}$$

Remarking that $\hat{y}(x)$ is also square-integrable, all the $\hat{y}_{i_1,\ldots,i_s}$ in Eq. (18) are also square-integrable, and, because of the orthogonality of the decomposition in Eq. (17), we obtain

$$\int_\Omega \hat{y}^2(x)\mathrm{d}x = \hat{y}_0^2 + \sum_i \int_\Omega \hat{y}_i^2(x_i)\mathrm{d}x_i + \sum_{i<j}\int_\Omega \hat{y}_{ij}^2(x_i, x_j)\mathrm{d}x_i, \mathrm{d}x_j + \cdots + \int_\Omega \hat{y}_{12,\ldots,P}^2(x_1, x_2, \ldots, x_P)\mathrm{d}x_1, \mathrm{d}x_2, \ldots, \mathrm{d}x_P \tag{20}$$

We compute the total and partial variances as

$$D = \int_\Omega \hat{y}^2(x)\mathrm{d}x - \hat{y}_0^2 \quad \text{and} \quad D_{i_1,\ldots,i_s} = \int_\Omega \hat{y}_{i_1,\ldots,i_s}^2(x_{i_1}, \ldots, x_{i_s})\mathrm{d}x_{i_1}, \ldots, \mathrm{d}x_{i_s} \tag{21}$$

where

$$D = \sum_{s=1}^{P}\sum_{i_1<\cdots<i_s}^{P} D_{i_1,\ldots,i_s}$$

The global sensitivity indices (also called Sobol' indices), defined as

$$S_{i_1,\ldots,i_s} = \frac{D_{i_1,\ldots,i_s}}{D} \tag{22}$$

represent the contribution of variable i (respectively, of the interaction between variables i and j, etc.) to the global variance (i.e., the sensitivity of the objective function to the design variables and their first- and higher-order interactions).

To compute the coefficients of Eq. (22), we used the 51^3 Cartesian kriging interpolation of Fig. 14, thus replacing continuous integrals with discrete sums (a thorough grid convergence study was also performed to ensure that the results were independent of our choice of hypercube size). This yields the decomposition of Fig. 20. It is interesting to note that the position of the actuation point, x_{inj}, barely contributes to lift variations by itself, contrary to δ_{inj} or, to a lesser extent, V_{inj}. This is confirmed by the plot of lift evolution relative to its average value against the single-design-variable effects displayed in Fig. 21 and is indicative of the Coandà-like mechanisms governing separation management (as will also be seen later on in a more detailed analysis), with a clear tendency toward increased lift as a result of increased momentum input and actuator deflection angle.

A look at two-way interactions in Fig. 22, in which the variations of lift coefficient with respect to its total average are represented, shows that their main contributions to lift variations lie in the strong relations between $x_{\text{inj}} - \delta_{\text{inj}}$ and $\delta_{\text{inj}} - V_{\text{inj}}$ (driven mainly by the zeroth-order influence of δ_{inj}). The three-way interaction, representing 12.8% of the total variation, is relatively low, which suggests that the dimensionality of our optimization problem could have been reduced from the beginning to a two-variable formulation.

For instance, should we simply account for x_{inj} and δ_{inj}, their zeroth- and first-order contributions would add up to 55.6% of the total variance already. Browsing for maximal lift on the kriging model (using GADO) at a constant and average injection velocity results in a value that is 10% lower than the optimum discussed

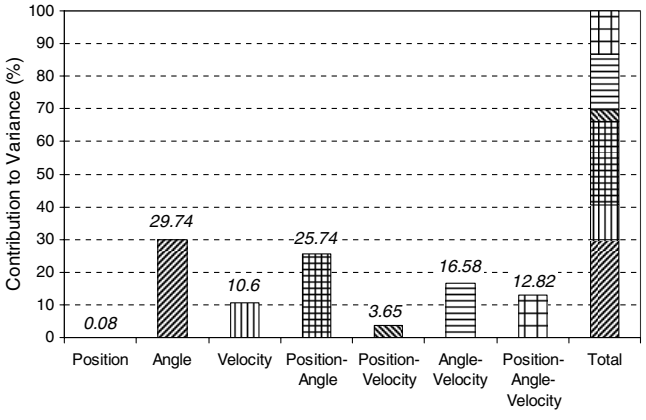

Fig. 20 ANOVA decomposition and contributions to total variance.

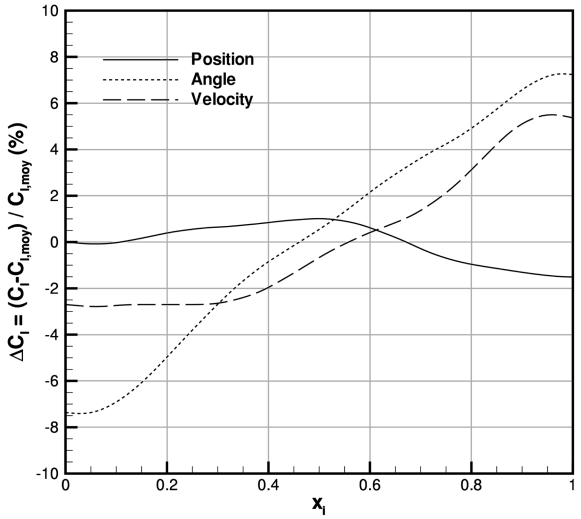

Fig. 21 Average contributions of single design variables to lift variations.

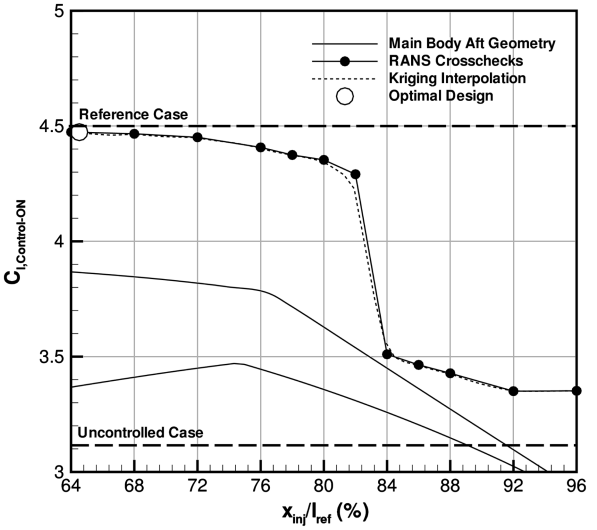

Fig. 23 Influence of injection location of the controlled lift, departure from the optimal design.

previously. Running the same computation at maximum velocity reduced this difference to less than 5%. Similarly, considering simply δ_{inj} and V_{inj} produces 56.9% of the total variance and yields a lift value that is only 2% smaller than its optimum for an average injection abscissa (remembering that x_{inj} does not have much influence on the evolution of the objective function).

Retaining the three design variables while neglecting their second-order interaction and considering the two couples $x_{inj} - \delta_{inj}$ and $\delta_{inj} - V_{inj}$ represents 82.7% of the total variance. An adaptation of Nash [56] noncooperative games (see Wang et al. [57] for an example) was performed on this biobjective problem and returned the exact optimal lift value.

Reducing the number of design variables has several advantages, especially with the surrogate-based procedure employed in this study:

1) The size of the original sampling population, N, being directly a function of the number of design parameters P ($N = k^P$), can be decreased drastically in a smaller-dimension hypercube, with important gains in the initial computational times and costs.

2) The number of hyperparameters defining the kriging model is equal to $P + 2$, where P is the number of design variables. Hence, the cost involved in the computation of the correlation relationship is largely affected by its dimensions. Furthermore, and because it is nothing but a minimization procedure treated using standard optimization techniques, the tuning of these parameters will become increasingly difficult as their quantity is increased, up to a point at which the model will completely loose its viability.

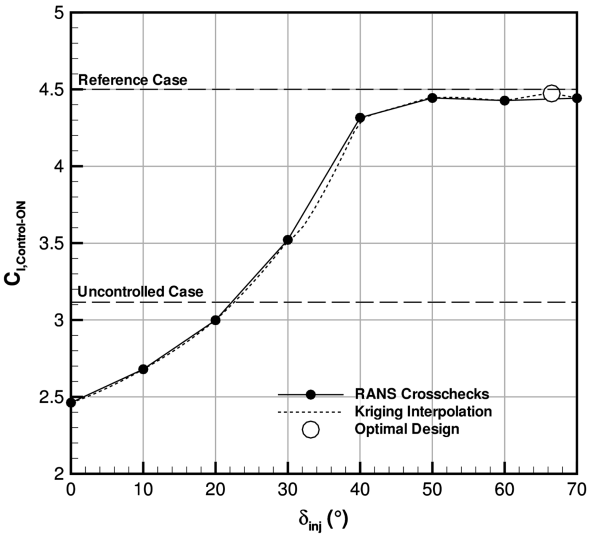

Fig. 24 Influence of injection angle of the controlled lift, departure from the optimal design.

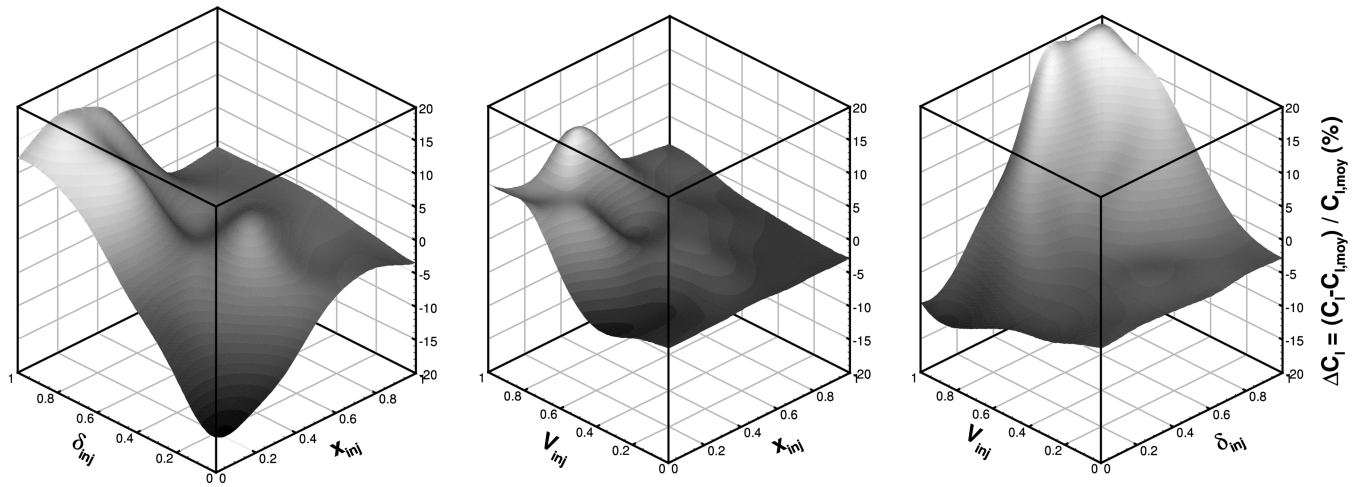

Fig. 22 Two-way interactions and average contributions to lift variations.

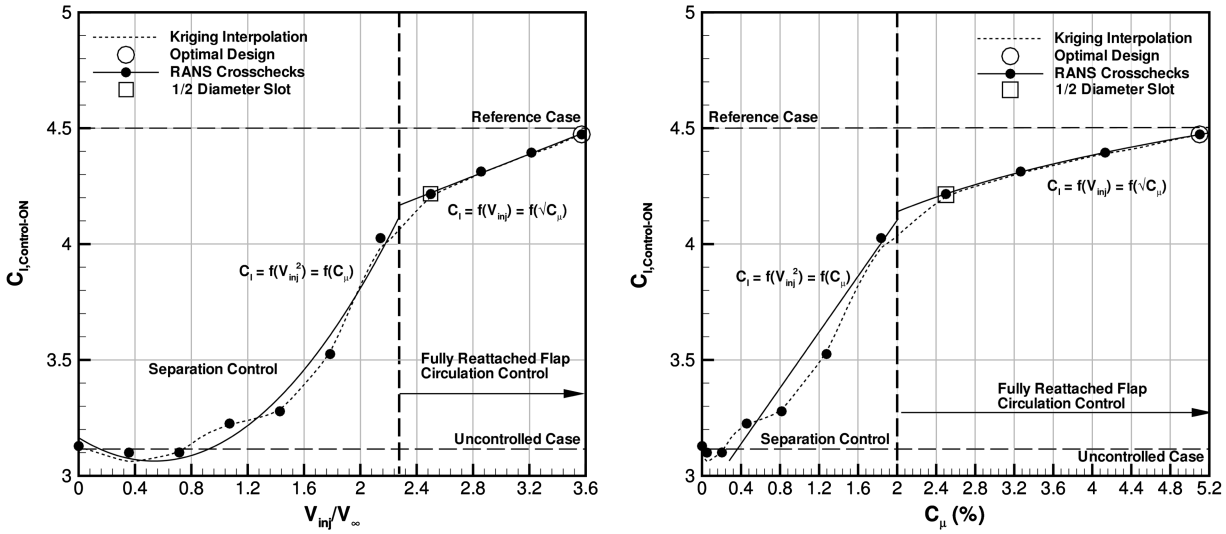

Fig. 25 Influence of injection momentum of the controlled lift, departure from the optimal design.

3) Eventually, which is even more true with weakly nonlinear engineering problems presenting smooth evolutions, the representation of the objective function is likely to become more rapidly (that is, with less samples) accurate as the number of design variables is reduced, allowing for less optimization iterations to be performed to reach convergence of both the metamodel and the optimal design.

5. Offdesign Behavior

Experimental (and, later, industrial) constraints will inevitably impose several other limitations on the parameterization of the control input. The optimal value of C_μ presented in Eq. (16) is far from being realistic for flight applications to be considered (for a classical three-engine business jet, such requirements would represent around 15% of the total available mass flow), whereas the optimal position identified by the preceding procedure does not account for the presence of fuel in the center parts of aircraft wings, etc. To try to evaluate the influence of a deviation of each design variable from its reference, a parametric study was conducted around the optimum point, at which the injection velocity, angle, and position were varied individually inside their respective ranges.

The influence of blowing positioning is depicted in Fig. 23. It can be seen that this parameter has a relatively limited influence on lift recovery over most of the available range of variation, as was expected from the average effects reported during the variance analysis. Control remains effective in suppressing the separation up to $x_{\text{inj}}/l_{\text{ref}} = 83\%$, well inside the uncontrolled recirculation area (for which separation occurs just behind the flap shoulder, at $x_{\text{inj}}/l_{\text{ref}} = 76\%$). The lift increment observed below this value is a consequence of increased suction and circulation due to the high-momentum near-surface wake of the jet. The kriging interpolation, extracted from the hypercube of Fig. 12 at the end of the optimization, is also seen to be in very good agreement with the RANS evaluations, indicative of the good quality of the model.

When looking at angle effects (Fig. 24), three trends can be observed. The first one, below approximately $\delta_{\text{inj}} = 22$ deg (up to the uncontrolled lift coefficient in fact), displays a lift increase that is easily explained by the fact that as deflection angle is increased (recalling that the values given here are referenced with respect to the surface normal), the contribution of the jet to negative lift decreases. Then, up to $\delta_{\text{inj}} = 40$ deg, the Coandà-like control starts building up as the wake of the jet progressively enters the existing boundary layer. Eventually, beyond $\delta_{\text{inj}} = 40$ deg, a saturation is observed, because the aforementioned effect is already completely established and does not leave any margin for performance improvements.

The effects of injection velocity are depicted in Fig. 25. Below $V_{\text{inj}}/V_\infty = 2.35$, and in the region that we refer to as separation control, increasing velocity results in decreasing the overall recirculation length of Fig. 9. The variation of lift coefficient is almost quadratic with V_{inj} (i.e., linear with C_μ), as is commonly observed in control problems involving steady actuation [18,26,58]. When the flap is fully reattached, the augmentation of lift with injection ratio is purely due to circulation control (increased suction level combined with amplified trailing-edge downwash). The evolution of lift then becomes linear with V_{inj}, as also reported by Loth [59].

IV. Conclusions

A surrogate-based automated framework for the optimization of flow-control-equipped configurations using overset grids is proposed and discussed. The tool was successfully applied to the challenging case of a two-dimensional airfoil with a simply hinged flap and equipped with constant blowing actuation, with the aim of maximizing lift in landing conditions. A complete reattachment of the flap flow was achieved, with an almost total recovery of the aerodynamic efficiency when compared with a conventional, fully slotted, reference geometry.

A Coandà-like circulation augmentation was identified as the main source of performance increase and calls for further investigations, mostly to try to minimize mass flow requirements (the most important parameter for possible in-flight applications). Consequently, future studies will also include the unsteady multiobjective (taking instantaneous variations as well as average lift levels into account) optimization of periodically blowing actuators (simulating pulsed or synthetic jets, or slots) to evaluate the resulting lift-loss penalty against power, pressure, or air-consumption benefits. Closed-loop forms of control, in which the entire dynamic and hysteresis impacts of the process are taken into account, also show great promises for input reductions relative to open-loop designs and should be conjointly considered.

Eventually, the possible application of flow control strategies could be assessed on more realistic three-dimensional cases, based on the general results obtained during simpler and less expensive two-dimensional parametric surveys, such as the one proposed and validated here.

Acknowledgments

Parts of this study were conducted in the frame of a national program supported by French government agencies Direction des Programmes Aéronautiques Civils (DPAC). The author would like to thank D. Bailly for the kriging model, as well as G. Carrier and I. Salah El Din for their help. The comments and reviewing efforts of P. Guillen, J. Reneaux, and P. Sagaut are also sincerely acknowledged.

References

[1] Gad-el-Hak, M., *Flow Control: Passive, Active and Reactive Flow Management*, Cambridge Univ. Press, Cambridge, England, U.K., 2000.

[2] Kral, L. D., "*Active Flow Control Technology*," American Society of Mechanical Engineers, Fluids Engineering Div., http://files.asme.org/Divisions/FED/16309.pdf [retrieved 26 Feb. 2009].

[3] Greenblatt, D., and Wygnanski, I., "The Control of Flow Separation by Periodic Excitation," *Progress in Aerospace Sciences*, Vol. 36, No. 7, 2000, pp. 487–545. doi:10.1016/S0376-0421(00)00008-7

[4] McLean, J. D., Crouch, J. D., Stoner, R. C., Sakurai, S., and Seidel, G. E., "Study of the Application of Separation Control by Unsteady Excitation to Civil Transport Aircraft," NASA Langley Research Center, CR-1999-209338, Hampton, VA, 1999.

[5] Meunier, M., and Brunet, V., "High-Lift Devices Performance Enhancement Using Mechanical and Air-Jet Vortex Generators," *Journal of Aircraft*, Vol. 45, No. 6, 2008, pp. 2049–2061. doi:10.2514/1.36836

[6] Seifert, A., Bachar, T., Koss, D., Shepshelovich, M., and Wygnanski, I., "Oscillatory Blowing: A Tool to Delay Boundary-Layer Separation," *AIAA Journal*, Vol. 31, No. 11, Nov. 1993, pp. 2052–2060. doi:10.2514/3.49121

[7] Nishri, B., and Wygnanski, I., "Effects of Periodic Excitation on Turbulent Flow Separation from a Flap," *AIAA Journal*, Vol. 36, No. 4, Apr. 1998, pp. 547–556. doi:10.2514/2.428

[8] Darabi, A., and Wygnanski, I., "Active Management of Naturally Separated Flow over a Solid Surface. Part 1. The Forced Reattachment Process," *Journal of Fluid Mechanics*, Vol. 510, 2004, pp. 105–129. doi:10.1017/S0022112004009231

[9] Darabi, A., and Wygnanski, I., "Active Management of Naturally Separated Flow over a Solid Surface. Part 2. The Separation Process," *Journal of Fluid Mechanics*, Vol. 510, 2004, pp. 131–144. doi:10.1017/S0022112004009243

[10] Becker, R., King, R., Petz, R., and Nitsche, W., "Adaptive Closed-Loop Separation Control on a High-Lift Configuration Using Extremum Seeking," *AIAA Journal*, Vol. 45, No. 6, June 2007, pp. 1382–1392. doi:10.2514/1.24941

[11] Hassan, A., "Improving Flap Aerodynamics Using Oscillatory Jet Control," 21st AIAA Applied Aerodynamics Conference, Orlando, FL, AIAA Paper 2003-3664, June 2003.

[12] Dandois, J., Garnier, E., and Sagaut, P., "Numerical Simulation of Active Separation Control by Synthetic Jet," *Journal of Fluid Mechanics*, Vol. 574, Mar. 2007, pp. 25–58. doi:10.1017/S0022112006003995

[13] Greenblatt, D., "Dual Location Separation Control on a Semi-Span Wing," 23rd AIAA Applied Aerodynamics Conference, Toronto, CAN, AIAA Paper 2005-5085, June 2005.

[14] Greenblatt, D., and Washburn, A. E., "Influence of Finite Span and Sweep on Active Flow Control Efficacy," AIAA Paper 2007-4275, 25th AIAA Applied Aerodynamics Conference, Miami, FL, 25–28 June 2007.

[15] Galbraith, M., "Numerical Simulations of a High-Lift Airfoil Employing Active Flow Control," 44th AIAA Aerospace Sciences Meeting and Exhibit, Reno, NV, AIAA Paper 2006-0147, 9–12 Jan. 2006.

[16] Kiedaisch, J., Nagib, H., and Demanett, B., "Active Flow Control Applied to High-Lift Airfoils Utilizing Simple Flaps," 3rd AIAA Flow Control Conference, San Francisco, AIAA Paper 2006-2856, June 2006.

[17] Shmilovich, A., and Yadlin, Y., "Flow Control for the Systematic Buildup of High Lift Systems," 3rd AIAA Flow Control Conference, San Francisco, AIAA Paper 2006-2855, June 2006.

[18] Nagib, H., Kiedaisch, J., Reinhard, P., and Demanett, B., "Control Techniques for Flows with Large Separated Regions: A New Look at Scaling Parameters," 3rd AIAA Flow Control Conference, San Francisco, AIAA Paper 2006-2857, June 2006.

[19] Seifert, A., and Pack, L., "Effects of Sweep on Active Separation Control at High Reynolds Numbers," *Journal of Aircraft*, Vol. 40, No. 1, Jan.–Feb. 2003, pp. 120–126. doi:10.2514/2.3066

[20] Nagib, H., Kiedaisch, J., Reinhard, P., and Demanett, B., "Active Flow Control for High Lift Airfoils: Separation versus Circulation Control," 45th AIAA Aerospace Sciences Meeting and Exhibit, Reno, NV, AIAA Paper 2007-1119, Jan. 2007.

[21] Kiedaisch, J., Demanett, B., Reinhard, Paul, and Nagib, H., "Active Flow Control for High Lift Airfoils: Dynamic Flap Actuation," 45th AIAA Aerospace Sciences Meeting and Exhibit, Reno, NV, AIAA Paper 2007-1120, Jan. 2007.

[22] Pack Melton, L., Schaeffler, N. W., Yao, C-S., and Seifert, A., "Active Control of Flow Separation from Supercritical Airfoil Leading-Edge Flap Shoulder," *Journal of Aircraft*, Vol. 42, No. 5, Sept.–Oct. 2005, pp. 1142–1149. doi:10.2514/1.10294

[23] Pack Melton, L., Yao, C.-S., and Seifert, A., "Active Control of Separation from the Flap of a Supercritical Airfoil," *AIAA Journal*, Vol. 44, No. 1, Jan. 2006, pp. 34–41. doi:10.2514/1.12225

[24] Pack Melton, L., Yao, C.-S., and Seifert, A., "Application of Excitation from Multiple Locations on a Simplified High-Lift System," 2nd AIAA Flow Control Conference, Portland, OR, AIAA Paper 2004-2324, 2004.

[25] Khodadoust, A., and Washburn, A., "Active Control of Flow Separation on a High-Lift System with Slotted Flap at High Reynolds Number," 25th Applied Aerodynamics Conference, Miami, FL, AIAA Paper 2007-4424, June 2007.

[26] Khodadoust, A., and Shmilovich, A., "High Reynolds Number Simulations of Distributed Active Flow Control for a High-Lift System," 25th Applied Aerodynamics Conference, Miami, FL, AIAA Paper 2007-4423, June 2007.

[27] Smith, A. M. O., "High-Lift Aerodynamics," *Journal of Aircraft*, Vol. 12, No. 6, 1975, pp. 501–530. doi:10.2514/3.59830

[28] Duvigneau, R., and Visonneau, M., "Simulation and Optimization of Stall Control for an Airfoil with a Synthetic Jet," *Aerospace Science and Technology*, Vol. 10, Feb. 2006, pp. 279–287. doi:10.1016/j.ast.2006.01.002

[29] Huang, L., Huang, P., LeBeau, R., and Hauser, T., "Optimization of Airfoil Flow Control Using a Genetic Algorithm with Diversity Control," *Journal of Aircraft*, Vol. 44, No. 4, July–Aug. 2007, pp. 1337–1349. doi:10.2514/1.27020

[30] Jeong, S., Murayama, M., and Yamamoto, K., "Efficient Optimization Design Method Using Kriging Model," *Journal of Aircraft*, Vol. 42, No. 2, Mar.–Apr. 2005, pp. 413–419. doi:10.2514/1.6386

[31] Jouhaud, J.-C., Sagaut, P., Montagnac, M., and Laurenceau, J., "A Surrogate-Model Based Multidisciplinary Shape Optimization Method with Application to a 2D Subsonic Airfoil," *Computers and Fluids*, Vol. 36, No. 3, Mar. 2007, pp. 520–529. doi:10.1016/j.compfluid.2006.04.001

[32] Meunier, M., "Simulation and Optimization of Flow Control Strategies for Novel High-Lift Configurations," 25th AIAA Applied Aerodynamics Conference, Miami, FL, AIAA Paper 2007-4276, 2007.

[33] McKay, M. D., Beckman, R. J., and Conover, W. J., "A Comparison of Three Methods for Selecting Values of Input Variables in the Analysis of Output from a Computer Code," *Technometrics*, Vol. 21, No. 2, May 1979, pp. 239–245. doi:10.2307/1268522

[34] Swiler, L., Slepoy, R., and Giunta, A., "Evaluation of Sampling Methods in Constructing Response Surface Approximations," 47th AIAA/ASME/ASCE/AHS/ASC Structures, Structural Dynamics, and Materials Conference, Newport, RI, AIAA Paper 2006-1827, May 2006.

[35] Cambier, L., and Veuillot, J.-P., "Status of the elsA CFD Software for Flow Simulation and Multidisciplinary Applications," 46th AIAA Aerospace Sciences Meeting and Exhibits, Reno, NV, AIAA Paper 2008-0664, Jan. 2008.

[36] Jameson, A., Schmidt, W., and Turkel, E., "Numerical Simulation of the Euler Equation by Finite Volume Methods Using Runge-Kutta Time Stepping Schemes," 14th AIAA Fluid and Plasma Dynamics Conference, Palo-Alto, CA, AIAA Paper 1981-1259, June 1981.

[37] Spalart, P., and Allmaras, S., "A One Equation Turbulence Model for Aerodynamic Flows," *La Recherche Aérospatiale*, Vol. 1, No. 5, 1994, pp. 5–21.

[38] Moens, F., "ONERA-RANS Activities Carried Out for Eurolift W. P. 2.1," ONERA Rept. RT 81/03631 DAAP, Feb. 2003.

[39] Orr, M. J. L., "Recent Advances in Radial Basis Function Networks," Inst. for Adaptive and Neural Computation, Edinburgh Univ., Edinburgh, Scotland, U.K., http://www.anc.ed.ac.uk/rbf/papers/recad.ps

[40] Sacks, J., Welch, W. J., Mitchell, T. J., and Wynn, H. P., "Design and Analysis of Computer Experiments," *Statistical Science*, Vol. 4, No. 4, 1989, pp. 409–435. doi:10.1214/ss/1177012413

[41] Liu, J.-L., "Novel Taguchi-Simulated Annealing Method Applied to Airfoil and Wing Planform Optimization," *Journal of Aircraft*, Vol. 43, No. 1, Jan.–Feb. 2006, pp. 102–109. doi:10.2514/1.13234

[42] Rasheed, K., "GADO: A Genetic Algorithm for Continuous Design Optimization," Ph.D. Thesis, Department of Computer Science, Rutgers Univ., New Brunswick, NJ, 1998.

[43] Dargel, G., and Schnieder, H., "GARTEUR AD (AG08) Final Report," GARTEUR High Lift Action Group, Rept. TP043 Nov. 1989.

[44] Jones, D., Schonlau, M., and Welch, W., "Efficient Optimization of Expensive Black-Box Functions," *Journal of Global Optimization*, Vol. 13, No. 4, 1998, pp. 455–492. doi:10.1023/A:1008306431147

[45] Manie, F., Piccin, O., and Ray, J.-P., "Test Report of the 2D Model M1 in the ONERA F1 Wind Tunnel," GARTEUR High Lift Action Group, Rept. TP041, Oct. 1989.

[46] Wilcox, D., *Turbulence Modeling for CFD*, 2nd ed., DCW Industries, La Cañada, CA, 2004.

[47] Jones, W. P., and Launder, B. E., "The Prediction of Laminarization with a 2-Equation Model of Turbulence," *International Journal of Heat and Mass Transfer*, Vol. 15, No. 2, 1971, pp. 301–314.

[48] Menter, F. R., "Two-Equation Eddy-Viscocity Turbulence Models for Engineering Applications," 23rd Fluid Dynamics, Plasmadynamics and Laser Conference, Orlando, FL, AIAA Paper 1993-2906, July 1993.

[49] Gear, C. W., *Numerical Initial Value Problems in Ordinary Differential Equations*, Prentice–Hall, Upper Saddle River, NJ, 1971.

[50] Lawrence, C., Zhou, J., and Tits, A., "User's Guide for CFSQP Ver. 2.5: A C Code for Solving (Large Scale) Constrained Nonlinear (Minimax) Optimization Problems, Generating Iterates Satisfying All Inequality Constraints," Inst. for Systems Research, Univ. of Maryland, TR-94-16r1, College Park, MD, 1997.

[51] Carrier, G., *Single and Multi-Point Aerodynamic Optimizations of a Supersonic Transport Aircraft Wing Using Optimization Strategies Involving Adjoint Method and Genetic Algorithm*, European Research Community on Flow Turbulence and Combustion, Las Palmas, Spain, Apr. 2006.

[52] Meckesheimer, M., Booker, A., Barton, R., and Simpson, T., "Computationally Inexpensive Metamodel Assessment Strategies," *AIAA Journal*, Vol. 40, No. 10, Oct. 2002, pp. 2053–2060. doi:10.2514/2.1538

[53] Joslin, R. D., and Jones, G. S., *Applications of Circulation Control Technology*, Progress in Astronautics and Aeronautics Series, Vol. 214, AIAA, Reston, VA, 2006.

[54] Abramson, J., and Rogers, E., "High Speed Characteristics of Circulation Control Airfoils," 21st Aerospace Sciences Meeting and Exhibit, Reno, NV, AIAA Paper 1983-0265, Jan. 1983.

[55] Sobol', I. M., "Global Sensitivity Indices for Non Linear Mathematical Models and Their Monte Carlo Estimates," *Mathematics and Computers in Simulation*, Vol. 55, No. 1-3, 2001, pp. 271–280. doi:10.1016/S0378-4754(00)00270-6

[56] Nash, J. F., "Non-Cooperative Games," *Annals of Mathematics and Artificial Intelligence*, Vol. 54, No. 2, Sept. 1951, pp. 286–295.

[57] Wang, J., Wu, Y., and Periaux, J., "Combinatorial Optimization Using Genetic Algorithms and Game Theory for High Lift Configuration in Aerodynamics," 41st Aerospace Sciences Meeting and Exhibit, Reno, NV, AIAA Paper 2003-0295, Jan. 2003.

[58] Wygnanski, I., Chen, C., and Zakharin, B., "On the Parameters Governing Fluidic Control of Separation and Circulation," 46th Aerospace Sciences Meeting and Exhibit, Reno, NV, AIAA Paper 2008-0629, Jan. 2008.

[59] Loth, J. L., "Applications of Circulation Control Technology: Advantages of Combining BLC Suction with Circulation Control High-Lift Generation," *Progress in Astronautics and Aeronautics*, Vol. 214, AIAA, Reston, VA, 2006, pp. 3–21.

E. Livne
Associate Editor